frontiers | Frontiers in Built Environment

TYPE Original Research
PUBLISHED 08 January 2024
DOI 10.3389/fbuil.2023.1334090

OPEN ACCESS

EDITED BY
Hoang Bao Khoi Nguyen,
University of South Australia, Australia

REVIEWED BY
Md. Rajibul Karim,
University of South Australia, Australia
M. M. Younus Ali,
RMIT University, Australia

*CORRESPONDENCE
A. C. Bradley,
andrew.bradley@adelaide.edu.au
M. B. Jaksa,
mark.jaksa@adelaide.edu.au

RECEIVED 06 November 2023
ACCEPTED 18 December 2023
PUBLISHED 08 January 2024

CITATION
Bradley AC, Jaksa MB and Kuo YL (2024), Ground response of rolling dynamic compaction—a finite element modelling approach.
Front. Built Environ. 9:1334090.
doi: 10.3389/fbuil.2023.1334090

Ground response of rolling dynamic compaction—a finite element modelling approach

A. C. Bradley*, M. B. Jaksa* and Y. L. Kuo

School of Civil, Environmental and Mining Engineering, University of Adelaide, Adelaide, SA, Australia

Rolling dynamic compaction (RDC) technology utilises a heavy non-circular module (impact roller) to compact the underlying soil dynamically. The stresses imparted to the soil through this technique and the resulting vibrations, have been the subject of investigation in the field. A finite element (FE) model predicting the settlement and densification of a coarse-grained fill material subject to RDC with a BH-1300 4-sided 8 tonne impact roller has been shown to provide good agreement with that observed in the field. This paper presents estimates using the developed FE model for the peak particle velocity and acceleration, and the maximum stresses applied through each impact upon a coarse-grained soil. Distributions of the results and their empirical formulae are presented herein.

KEYWORDS

rolling dynamic compaction, impact roller, granular materials, vibration, finite element

1 Introduction

Rolling dynamic compaction (RDC) technology involves the use of a heavy non-cylindrical rolling module incorporating 3, 4 or 5 sides. The module is typically towed at a speed of 10–12 km/h. The module consequently pivots about its corners to impact the soil along its face. Through this technique, a substantial amount of energy is delivered to the ground with each impact. Imparting stress and vibration, RDC can be utilised to improve the bearing capacity of underlying soils at depth for a specified number of passes (N). However, the stress at depth and resulting vibration, in terms of peak particle velocity (PPV) and peak particle acceleration (PPA) during RDC, may be hazardous or unsuitable at specific sites, especially with brittle or vulnerable nearby structures. Understanding the extent to which RDC affects its surroundings will improve the success of future applications.

Within the literature, the maximum vertical stress applied, and the *in-situ* vibration of the soil, have been modestly investigated in the field. These were carried out with the use of Earth pressure cells (EPCs) and *in-situ* accelerometers, as summarised in Table 1.

In their field investigations using EPCs at 0.7 and 1.1 m depth, respectively, Scott et al. (2016) and Scott et al. (2019a) reported a significant range of estimates for the peak vertical stress less the initial overburden, and the PPA at depth, as summarised in Table 2. The significant variability of the stress and PPA measured by Scott et al. (2016) and Scott et al. (2019a) is likely borne from a combination of factors, including but not limited to: sampling frequency and resolution, and the kinematic behaviour of the roller whereby the roller may engage in erratic "skipping motion." Further, the first 50 passes appear to be markedly lower, inferring that the response is, understandably, dependent on the progression of the densification of the subsoil.

Research on the ground vibrations along the surface due to RDC is exclusive to that presented by Avalle (2007), as shown in Figure 1, where the surface vibration with respect to

distance, across a variety of site conditions and literature, is presented. Moreover, Avalle (2007) presented the results with reference to "safe" levels of vibration as specified by the BS 7385-2: 1993 (British Standards, 1993) and DIN 4150-3: 1999 (Deutsche Norm, 1999) standards.

Subject to initial conditions and limitations, a finite element (FE) model can provide insight to the distribution and magnitude of the effectiveness of RDC on an underlying soil. In their effort to investigate the effectiveness of RDC, with a BH-1300 4-sided 8-tonne impact roller, Bradley et al. (2023) developed a FE model, using LS-DYNA (LSTC, 2015), that reproduced, with good agreement, the settlement and densification of a coarse-grained soil. Following their methodology, the kinematics and energy of the roller are representative of *typical motion* as observed in the field by Bradley et al. (2019).

TABLE 1 Studies of 4-sided impact roller reporting PPA, PPV, and *in-situ* stress history.

Study	Soil	Passes	S	DCP	CPT	PPV/A	SGT	ND	SR	EPC
Avalle and Young (2004)	Fill	30	Y		Y	Y				
Avalle and McKenzie (2005)	Fill	48	Y			Y	Y			
Bouazza and Avalle (2006)	Fill	48				Y	Y			
Avalle (2007)	Various	—				Y				
Avalle et al. (2009)	Fill	18	Y			Y				Y
Jaksa et al. (2012)	Sand (TP)	16		Y					Y	Y
Scott et al. (2016)	Sandy Gravel	80	Y	Y		Y	Y	Y		Y
Scott et al. (2019a)	Sandy Gravel	80				Y				Y
Scott et al. (2019b)	Sand (TP)	16	Y	Y			Y		Y	Y
Scott et al. (2020)	Sandy Gravel	40, 100								Y

Note: S, Surface Settlement measured; DCP, Dynamic Cone Penetrometer test; CPT, Cone Penetration Test; PPV/A, Peak Particle Velocity/Acceleration; TP, Test Pad; SGT, Seismic Geophysical Techniques; ND, Nuclear Densometer test; SR, Sand Replacement test; EPC, Earth Pressure Cell.

TABLE 2 Summary of peak ground response study per pass by Scott et al. (2016) and Scott et al. (2019a).

Study	Depth (m)	Peak EPC (kPa)			PPA (g's)		
		Min	Average[a]	Max	Min	Average[a]	Max
Scott et al. (2019a)	0.7	166	461 ± 95	1,115	1.3	6.3 ± 1.3	13.2
Scott et al. (2016)	1.1	131	377 ± 32	716	0.8	3.4 ± 0.4	10.5

[a]At 95% confidence.

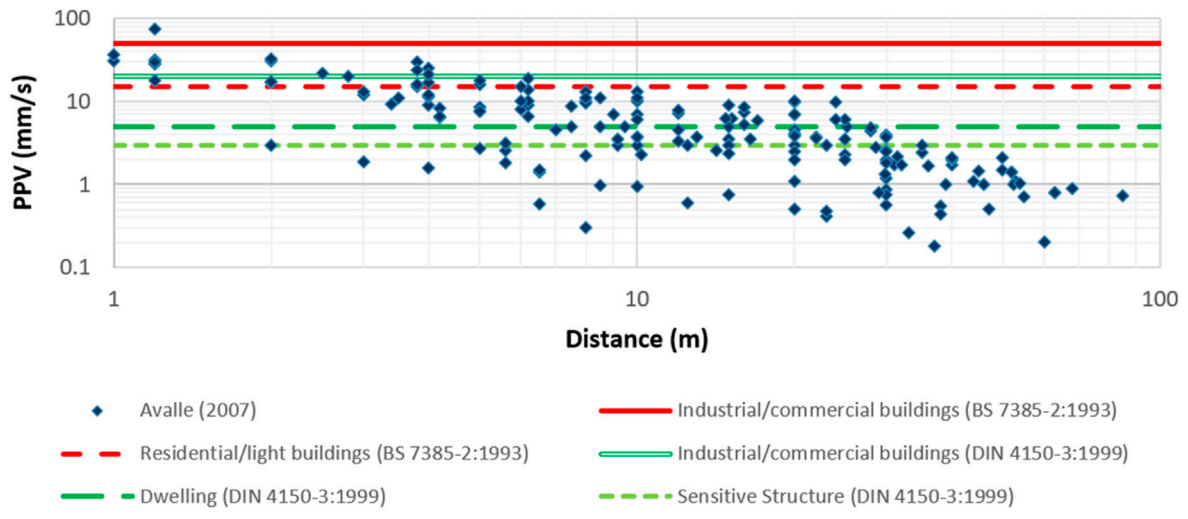

FIGURE 1
Vibration results for 25 case study sites (after Avalle, 2007).

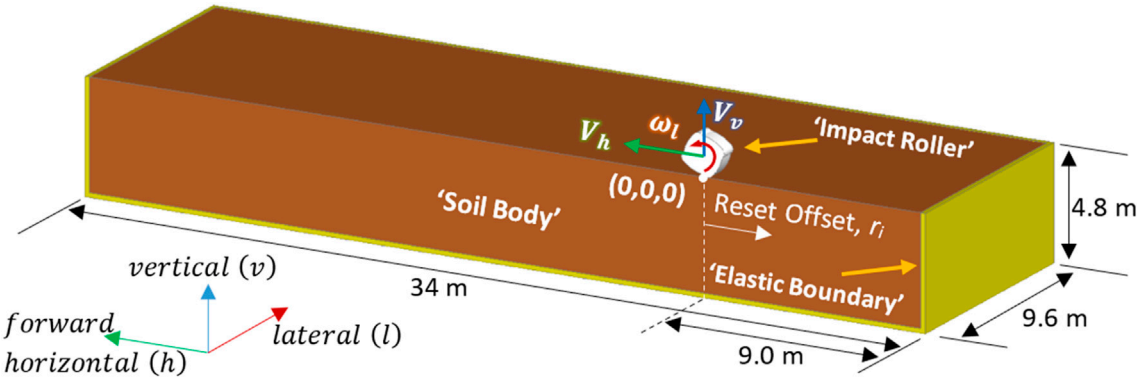

FIGURE 2
Global model layout in LS-DYNA (Bradley et al., 2023).

This paper aims to explore the peak ground response of RDC of the BH-1300 4-sided 8-tonne impact roller using the FE model presented by Bradley et al. (2023). Firstly, estimates for the peak cartesian stresses, and mean pressure are presented, including the horizontal distribution of the peak vertical stress. Secondly, the PPA and PPV are examined, initially with respect to depth, and then for along the soil surface. The model predictions are benchmarked against field measurements available within the literature.

2 Methodology

A FE analysis is performed, using LS-DYNA, involving the 4-sided 8-tonne impact roller undertaking $N = 30$ passes, with 10 impacts per pass, using the FE model formulation and methodology as presented by Bradley et al. (2023), as shown in Figure 2. To ensure confidence in capturing the peak values, the FE simulations are performed at an elevated sample frequency of 1 kHz.

Bradley et al. (2023) examined the numerical efficacy of two FE mesh resolutions, namely, $100\,mm \times 100\,mm \times 100\,mm$ and $200\,mm \times 200\,mm \times 200\,mm$. Understandably, the authors observed improved performance with the finer mesh. However, in the context of the present ground vibration analyses, the coarser FE mesh resolution is selected. Given the significantly increased sampling frequency, simulating and post-processing the finer mesh would incur exponentially greater resource and time demands, which are well-beyond the scope of this study.

As explained by Bradley et al. (2023), at the beginning of each subsequent pass, the module is returned to the start of the lane, with respect to the initial position of the roller in Figure 2. To distribute the disturbance of the surface soils upon dropping of the module during the resetting phase, and to simulate the somewhat random positioning of the roller that occurs in the field, a variable reset offset (r_i), is adopted in the FE model simulations. The values of r_i used by Bradley et al. (2023) are also adopted in this study.

As also explained by Bradley et al. (2023), a constant downward vertical loading (L) is applied to the nodes of the roller to represent the vertical contribution of load through the double-linkage spring mechanism of the roller to better represent the somewhat complex nature of the roller's motion. Within this study, $L = 0.25$ N is considered.

The characteristics of the soil adopted in the FE model is identical to that specified by Bradley et al. (2023), from their field trial, reproduced in Table 3; however, in order to model a coarse-grained soil with no fines content, i.e., a cohesionless material, effective cohesion (c') = 1 kPa. Bradley et al. (2023) performed particle size distribution tests (Standards Australia, 2009) on bulk samples of the fill material with a maximum particle size of no greater than 20 mm to describe their material as a poorly-graded sandy gravel with a trace of fines by the Unified Soil Classification System (USCS). Informed by a combination of dynamic cone penetration (DCP) (Standards Australia, 1997) and nuclear density meter testing (Standards Australia, 2007), the initial density (ρ_0) and initial dry density ($\rho_{d|0}$) of the fill, prior to RDC, the soil was reasonably homogenous throughout the lift. The specific gravity of the solids (G_s) of the fill material was estimated by Bradley et al. (2023) from 11 pycnometer tests (Standards Australia, 2006). Further, the maximum void ratio (e_{max}) of the fill material was estimated as per AS 1289.5.5.1 (Standards Australia, 1998). However, the minimum void ratio (e_{min}) of the fill material was selected by Bradley et al. (2023) as that associated with the maximum dry density from the modified Proctor test (Standards Australia, 2017). Hence, for a given dry density ($\rho_{d|0}$), the void ratio (e_0), and relative density (Dr_0) were thus calculated. Consolidated undrained triaxial compression tests (Standards Australia, 2016) were undertaken by Bradley et al. (2023) at varying confinements, and strain rates, to identify the critical state effective angle of friction (φ'_{cv}) and the apparent peak effective cohesion (c') of the fill material; thus allowing for the calculation of the Drucker-Prager cohesion (d') and slope (M). The volumetric behaviour of the fill material was investigated by Bradley et al. (2023) with 1D-compression tests (Standards Australia, 2020) to estimate the virgin compression line void ratio intercept (e_L), apparent preconsolidation pressure (p_c), logarithmic slopes of the unload–reload line (κ) and the virgin compression line (λ).

3 Results

A multiple pass scenario for $N = 30$ passes of the BH-1300, 8-tonne, 4-sided impact roller was successfully modelled. The motion of the roller produced within the FE model is well correlated with the field derived *typical motion* time history

TABLE 3 Summary of geotechnical parameters for fill material (Bradley et al., 2023).

USCS	ρ_0 (t/m^3)	$\rho_{d\|0}$ (t/m^3)	G_s (t/m^3)	e_0	e_{max}	e_{min}	Dr_0 (%)
GP	1.88	1.68	2.654	0.585	0.816	0.328	47.4
e_L	p_c (kPa)	κ	λ	c' (kPa)	φ'_{cv} (°)	d' (kPa)	M
0.850	197	0.0035	0.0537	13.5[a]	38.5	80[a]	1.57

[a]$c' = 1\,kPa$ is selected to represent cohesionless soil.

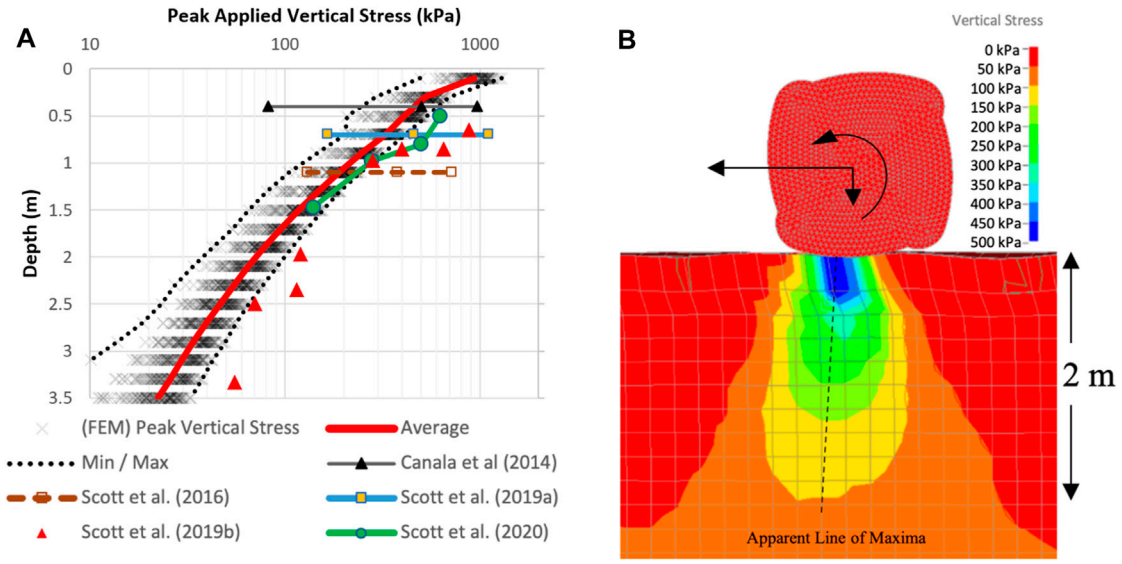

FIGURE 3
Peak vertical stresses: **(A)** Applied vertical stress (σ_v^A) with depth; and **(B)** Typical distribution of peak *in-situ* vertical stress (σ_v) during impact [N = 5].

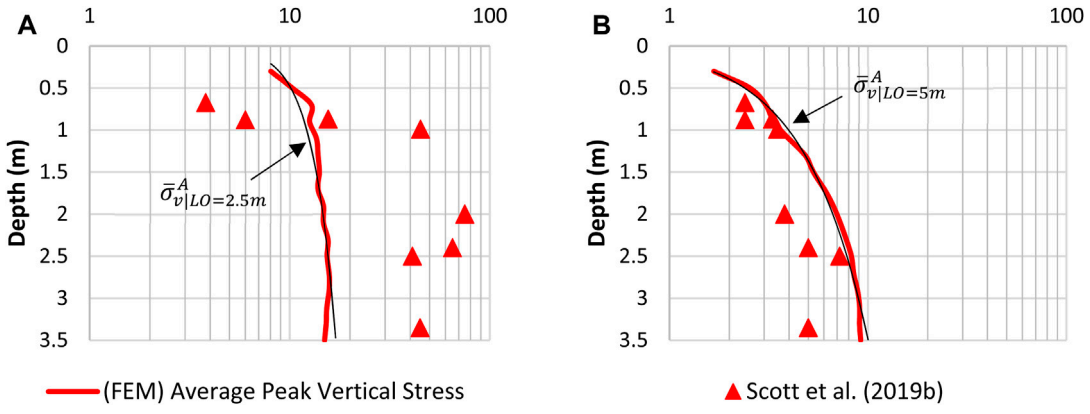

FIGURE 4
Peak applied vertical stress (σ_v^A) for lateral offsets: **(A)** 2.5 m; and **(B)** 5 m.

produced by Bradley et al. (2019); no "skipping motion" is present. With 95% confidence, the average peak kinetic energy of the roller through each impact is $64.4 \pm 0.3\,kJ$; the average energy loss of the roller through each impact is $24.8 \pm 0.6\,kJ$; and the average energy absorbed by the soil through each impact is $19.7 \pm 1.2\,kJ$. Hence, the motion of the roller was reasonably represented in accordance with the methodology by Bradley et al. (2023).

In the sub-sections that follow, firstly, results of the *in-situ* peak cartesian stresses are presented in Section 3.1 against field

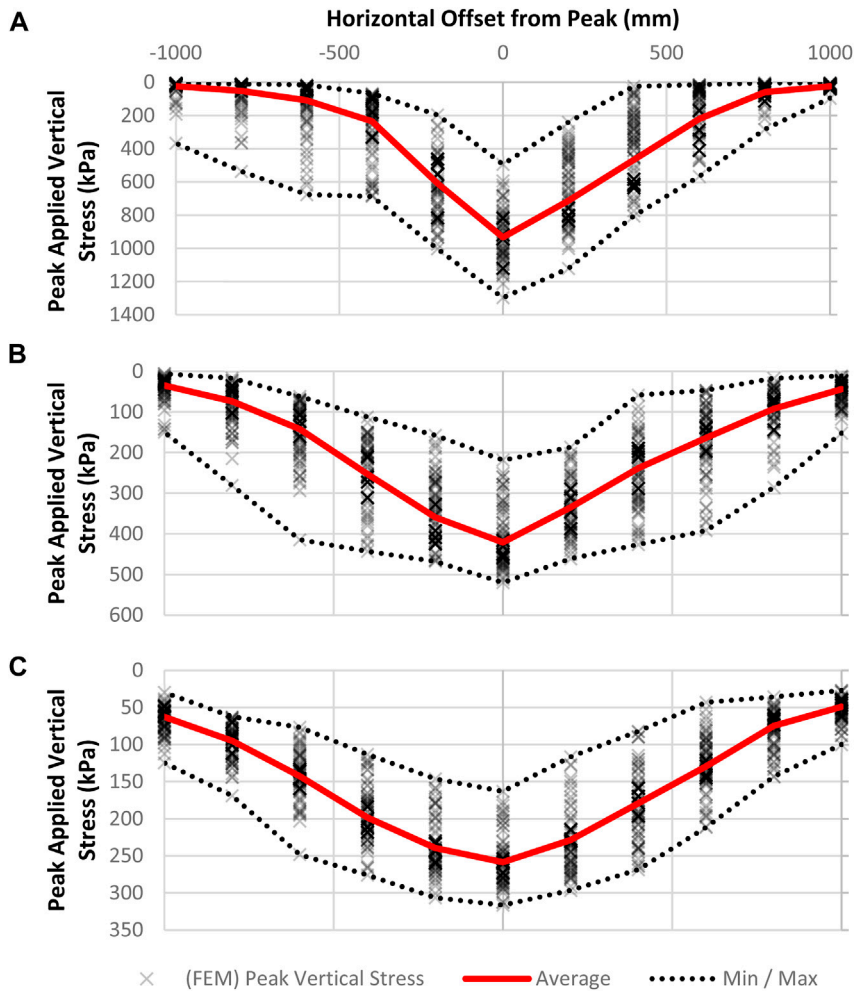

FIGURE 5
Horizontal distribution of peak *in-situ* applied vertical stress with each impact: **(A)** 0.1 m depth; **(B)** 0.5 m depth; and **(C)** 0.9 m depth.

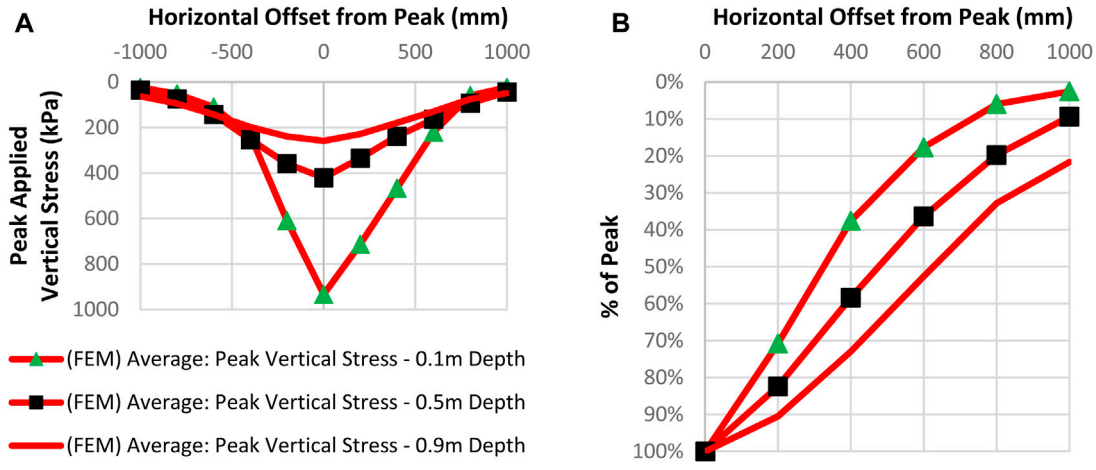

FIGURE 6
Distribution of average peak applied vertical stress: **(A)** Along the horizontal; and **(B)** Along the horizontal with respect to horizontal offset from the peak.

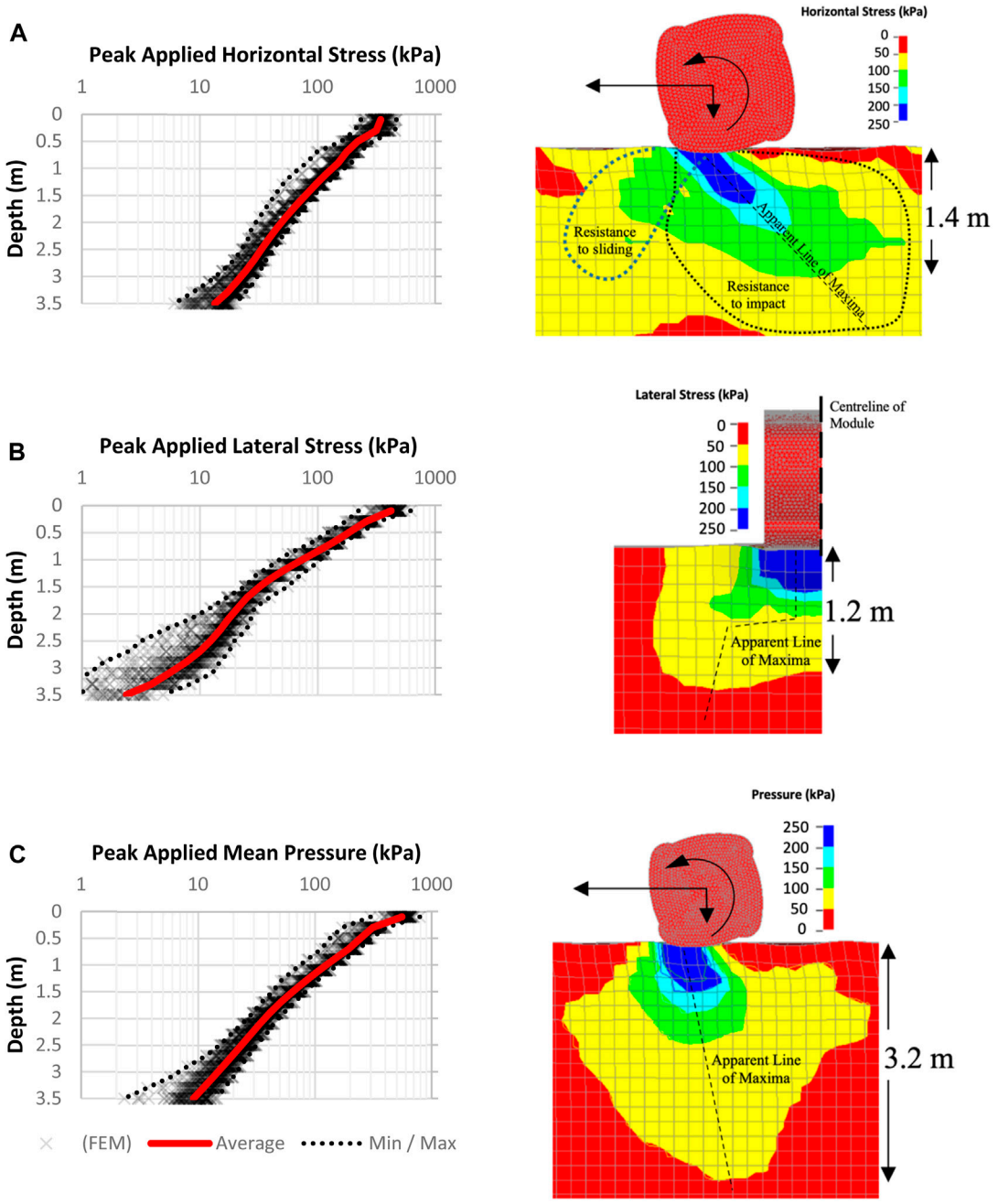

FIGURE 7
Summary of peak *in-situ* applied stresses and their typical distributions during impact: **(A)** σ_h^A; **(B)** σ_L^A; and **(C)** p^A.

observations available in the literature. Subsequently, in Section 3.2, the resulting ground vibration at depth, in terms of the PPV and PPA, are examined. Finally, in Section 3.3, the ground vibration along the soil surface is assessed with respect to lateral distance from the centreline of the target lane (D).

3.1 Peak applied *in-situ* stress

The peak applied *in-situ* stress is the peak stress less the initial stress at rest. The resulting peak applied vertical stress (σ_v^A) with respect to depth, for each impact for all 30 passes, is presented in Figure 3. Although the FE simulation appears to have modestly underestimated the peak σ_v^A within 1 m of the surface, there is still good agreement between the maximum σ_v^A estimated and field measurements reported by Scott et al. (2019a, 2019b, 2020). This is despite differences, between the setting in some of the field investigations and to that in the simulation.

The average of $\bar{\sigma}_v^A$ produced by the FE model along the lane, for all 30 passes, with respect to depth (d) is well represented by Eq. 1, and the maximum by Eq. 2.

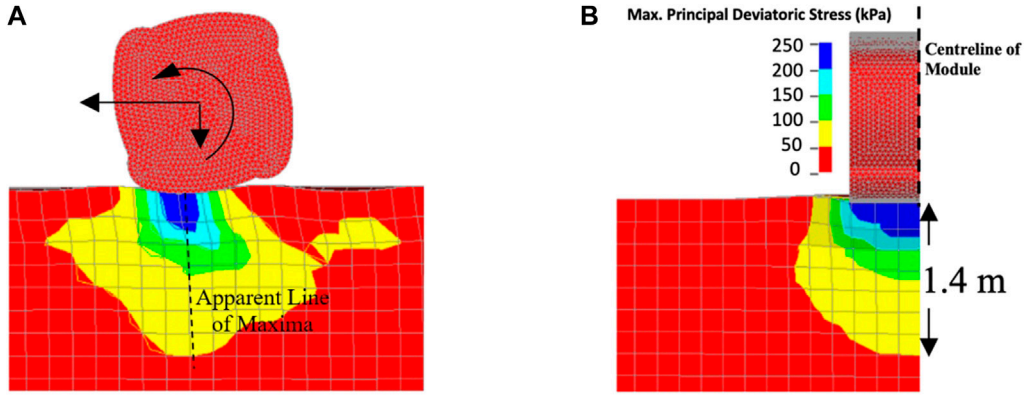

FIGURE 8
Typical distributions of maximum principal deviatoric stresses during impact: **(A)** horizontal; and **(B)** lateral.

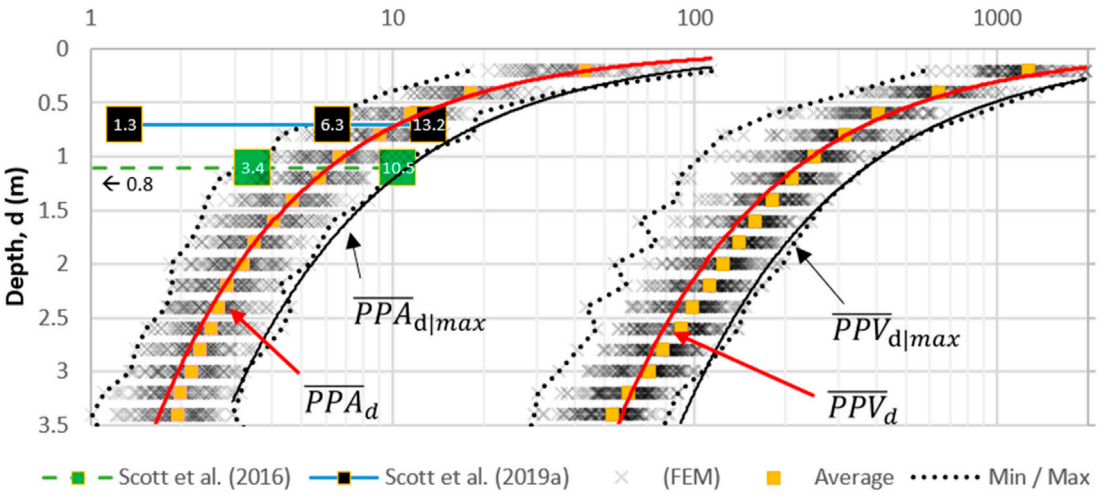

FIGURE 9
Summary of at depth PPA (in g); and PPV (in mm/s).

$$\bar{\sigma}_v^A = 730.495 \cdot e^{-1.101 \cdot d} \quad (1)$$

$$\bar{\sigma}_{v|max}^A = 894.711 \cdot e^{-1.029 \cdot d} \quad (2)$$

Additionally, σ_v^A with respect to varying lateral offsets (LO), is presented in Figure 4, with the field measurements reported by Scott et al. (2019b). The FE model reproduced the far field estimates for LO = 5 m, however the FE model did not necessarily reproduce the field measurements for LO = 2.5 m. The results are well fit by Eqs 3, 4.

$$\bar{\sigma}_{v|D=2.5m}^A = \frac{6087}{500} \cdot d^{0.266} \quad (3)$$

$$\bar{\sigma}_{v|D=5m}^A = \frac{498}{125} \cdot d^{0.737} \quad (4)$$

The distribution of σ_v^A along the lane and in the direction of rolling, for all 30 passes, is presented in Figure 5 at three different depths: 0.1, 0.5, and 0.9 m. These distributions illustrate the importance of the location and resolution of sampling relative to where greatest impact is applied. Figure 6 presents the results from Figure 5, superimposed onto a single plot and infers that a horizontal offset of 200 mm from the peak at 0.5 m depth may be underestimated by approximately 20%. This sensitivity of "hit or miss" is evident in the range of measurements reported within the literature. Nevertheless, majority of the loading per blow spans approximately 1 m, akin to the length of the impact face of the RDC module.

Although σ_v^A through RDC is an indicator for the extent of influence RDC has at depth, it is also important to consider the stress applied orthogonally to it and the mean pressure. The peak applied horizontal (σ_h^A) and lateral (σ_L^A) stress, in addition to the peak applied mean pressure (p^A), are presented in Figure 7. Their averages, for all 30 passes, with respect to depth is represented well by Eqs 5–7. The apparent line of maxima is notably acting at angles, as the kinetic compactive energy tends to be delivered underneath and behind the roller. This is likely a consequence of the contribution of the angular momentum of the RDC module within the complex interaction of each impact.

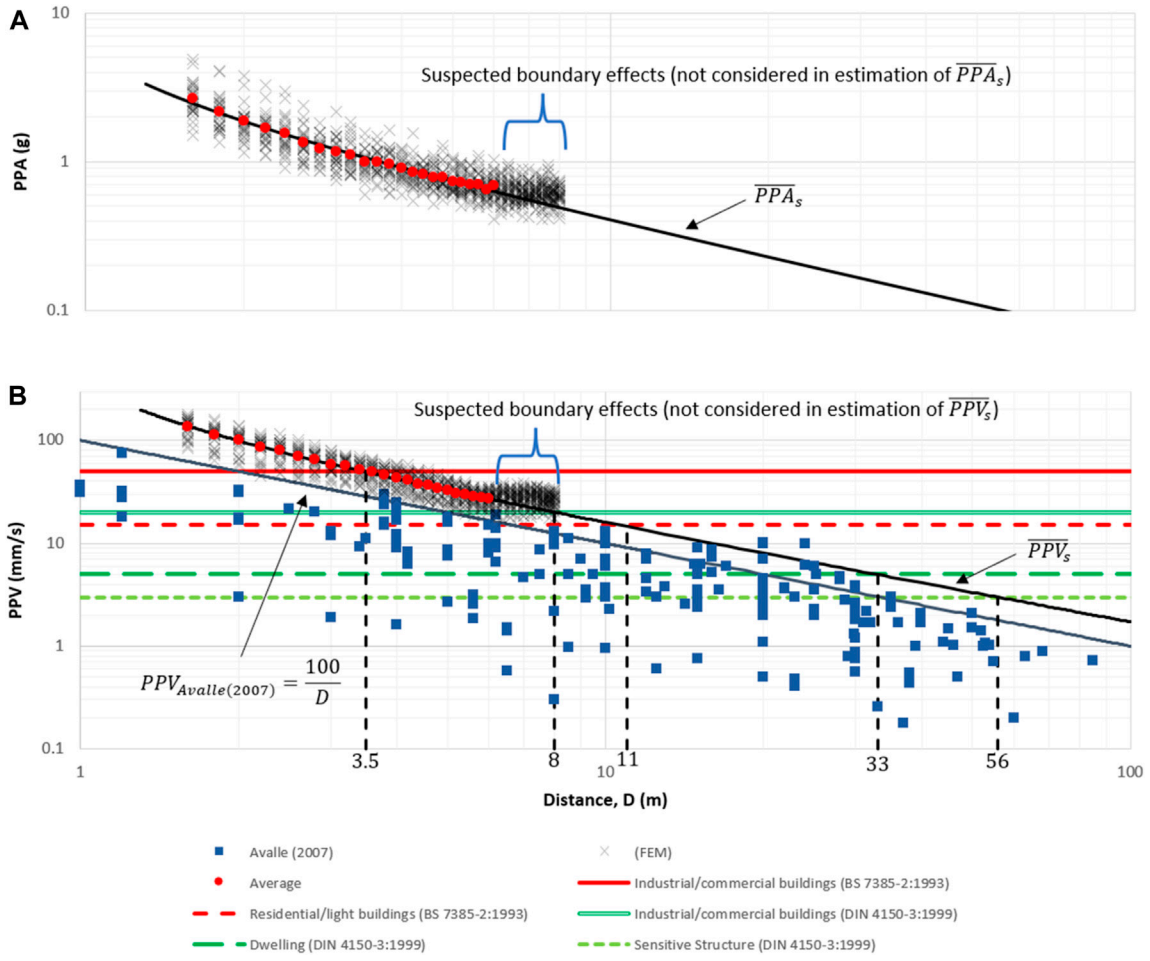

FIGURE 10
Surface peak particle: **(A)** acceleration; and **(B)** velocity.

$$\bar{\sigma}_h^A = 369.192 \cdot e^{-0.976 \cdot d} \quad (5)$$

$$\bar{\sigma}_L^A = 385.419 \cdot e^{-1.468 \cdot d} \quad (6)$$

$$\bar{p}^A = 455.484 \cdot e^{-1.193 \cdot d} \quad (7)$$

A feature of RDC is the disturbance of the near surface soils as the roller shears and dilates the surface material. Namely, this is a product of the magnitude of the shear stress applied through each impact exceeding the capacity of the soil to resist. Figure 8 presents the typical distribution of the maximum principal deviatoric stress through each impact.

3.2 Vibration at depth

Figure 9 presents the PPA and PPV values obtained at the nodes, for each impact across all 30 passes for $0.2 \le d \le 3.5\,m$. The PPA results fit well with the upper bound estimates measured in the field by Scott et al. (2016) and Scott et al. (2019a). The respective average and maximum PPAs and PPVs with depth are represented well by Eqs 8–11.

$$\overline{PPA}_d = 6.886 \cdot d^{-1.152} \quad (8)$$

$$\overline{PPV}_d = 243.439 \cdot d^{-1.181} \quad (9)$$

$$\overline{PPA}_{d|max} = 12.633 \cdot d^{-1.226} \quad (10)$$

$$\overline{PPV}_{d|max} = 412.246 \cdot d^{-1.215} \quad (11)$$

3.3 Surface vibration

In the previous section, the PPAs and PPVs with respect to depth were reported. In this section, the PPA and PPV along the ground surface with respect to the lateral distance (D) to the centreline of the lane subject to RDC are reported and presented in Figure 10. As can be seen, and as expected, the results suitably envelope the field data obtained by Avalle (2007). The idealisation of representing the soil in a FE simulation removes the imperfections and discontinuities that would otherwise retard, mitigate or reduce the PPA and PPV in the field. Nonetheless, the trends presented ought to provide a conservative upper estimate for PPA and PPV along the ground surface.

Upon further inspection, estimates at $D > 6\,m$ appear to be subject to boundary effects. This is despite a non-reflecting boundary being defined along the outer perimeter of the soil mass. One possible explanation is the soil mass is tied to an elastic boundary defined with a non-reflecting boundary condition. This is required within the model formulation of Bradley et al. (2023), as the constitutive model for the soil mass does not permit the use of a non-reflecting boundary condition along it directly, and so it must be incorporated indirectly. However, this approach would be imperfect, and the model would be subject to boundary effects along the interface between the soil mass and the elastic boundary. There is, however, no significant evidence to suggest the boundary effects extend any closer than $D = 6\,m$.

In maintaining a conservative approach with respect to erroneous disturbance resulting from RDC and the suspected presence of boundary effects, the trends for PPA and PPV are considered to be best estimated within the region $1.6 \leq D \leq 6\,m$, for all 30 passes. As is evident from Figure 10, the averages of the surface PPAs and PPVs are well represented by Eqs 12, 13.

$$\overline{PPA}_s = 2.375 \cdot (D - 0.65)^{-0.789} \tag{12}$$

$$\overline{PPV}_s = 132.032 \cdot (D - 0.65)^{-0.944} \tag{13}$$

4 Conclusion

This paper presented results of a FE simulation of RDC performed by a Broons BH-1300 4-sided 8-tonne impact roller on coarse-grained soil subjected up to 30 passes, using the formulation as presented by Bradley et al. (2023). These results have reasonably reproduced field observations available within the literature by use of the FE simulation approach. A greater understanding of the extent RDC has on the ground response is achievable with the use of FE simulations. Distributions and trends for the *in-situ* stresses were presented. Further, the PPA and PPV for at depth and along the surface were also presented.

However, there are limitations to consider when utilising the FE simulation approach. In the field, the imperfections, discontinuities, layering, and heterogeneity of soils are likely to impact the results by typically reducing the PPA and PPV at depth and along the surface. The idealisation of representing the soil in a FE simulation removes these imperfections. Therefore, trends presented herein, and any potential parametric studies utilising the FE simulation, are ought to provide a conservative upper estimate for PPA and PPV.

Another limitation is that the FE simulation considered the roller running along a single lane. In the field, RCD is undertaken with adjacent lanes, modifying the ground conditions lateral to each lane. The impact of the inclusion of adjacent lanes on the results is non-trivial and may be an area of future study. It is presumed the additional effective confinement of the soil due to compactive action in adjacent lanes would attribute to a larger applied stress and ergo performance. This may provide an explanation as to why the peak applied vertical stress in the upper 1 m below the roller and at the intermediate lateral offset of 2.5 m was not necessarily reproduced, Figure 3 and Figure 4. Nevertheless, the FE simulation presents a reasonable reproduction of the average stresses as observed in the field. However, the peak values of stress in the upper 1 m are likely underestimated and may require to be increased by a factor of 2.

The results presented herein are reflective of the use of the course $200\,mm \times 200\,mm \times 200\,mm$ FE mesh resolution. Improved results may be obtained with a finer FE mesh resolution, but at greater computational cost. Boundary effects were also identified within the model. This suggests either the width of the soil mass may need to be increased or another approach is needed to better mitigate the boundary effects when investigating far-field estimates.

Ideally with a field or scale-model investigation, future studies would be served well by a robust investigation utilising the FE simulation approach with respect to varying soil conditions. Further, there is room to improve upon Bradley et al. (2023)'s model formulation. Multiple distinct layers, in place of a homogenous soil mass, each with their own geotechnical characteristics and behaviour, as is typically the case in the field, is one such consideration.

Data availability statement

The original contributions presented in the study are included in the article/Supplementary Material, further inquiries can be directed to the corresponding authors.

Author contributions

AB: Conceptualization, Data curation, Formal Analysis, Investigation, Methodology, Software, Writing–original draft. MJ: Supervision, Writing–review and editing. YK: Supervision, Writing–review and editing.

Funding

The author(s) declare that no financial support was received for the research, authorship, and/or publication of this article.

Acknowledgments

The authors appreciate the assistance of Dr. Brendan Scott and Mr. Mark Innes at the University of Adelaide. The authors are grateful for the support team for the Phoenix High Performance Computing services at the University of Adelaide.

Conflict of interest

The authors declare that the research was conducted in the absence of any commercial or financial relationships that could be construed as a potential conflict of interest.

Publisher's note

References

Avalle, D. L. (2007). "Ground vibrations during impact rolling," in Common Ground Proceedings 10th Australia New Zealand Conference on Geomechanics, Brisbane, Australia, 21-24 October 2007.

Avalle, D. L., Jaksa, M., and Scott, B. (2009). "Ground energy and impact of rolling dynamic compaction - results from research test site," in 17th International Conference on Soil Mechanics and Geotechnical Engineering, Alexandria, Egypt, 5-9 October 2009 (IOS Press). doi:10.3233/978-1-60750-031-5-2228

Avalle, D. L., and McKenzie, R. W. (2005). Ground improvement of landfill site using the "square" impact roller. *Aust. Geomech.* 40 (4), 15–21.

Avalle, D. L., and Young, G. (2004). "Trial programme and recent use of the impact roller in sydney," in *In earthworks seminar* (Adelaide, Australia: Australian Geomechnics Society), 1–5.

Bouazza, A., and Avalle, D. L. (2006). Verification of the effects of rolling dynamic compaction using a continuous surface wave system. *Aust. Geomech.* 41 (2), 101–108.

Bradley, A. C., Jaksa, M. B., and Kuo, Y. L. (2019). Examining the kinematics and energy of the four-sided impact roller. *Proc. Institution Civ. Eng. - Ground Improv.* 172 (4), 297–304. doi:10.1680/jgrim.18.00124

Bradley, A. C., Jaksa, M. B., and Kuo, Y. L. (2023). Finite element modelling of rolling dynamic compaction. *Comput. Geotechnics* 157, 105275. doi:10.1016/j.compgeo.2023.105275

British Standards (1993). *BS 7385 Evaluation and measurement for vibration in buildings. Part 2: guide to damage levels from groundborne vibration*. UK: BSI.

Canala, G. S., Gauro, C. A., March, J. C., and Strapps, R. W. (2014). *Final Research Project Report: quantifying the effectiveness of the four-sided impact roller with operating speed*. Adelaide, Australia: University of Adelaide.

Chung, O. Y., Scott, B. T., Jaksa, M. B., and Kuo, Y. L. (2017). "Physical modeling of rolling dynamic compaction," in Proc. of 19th Internation Conference on Soil Mechanics and Geotechnical Engineering, Seoul, South Korea, 17-22 September 2017, 905–908.

Deutsche Norm (1999). *DIN 4150 Structural vibration. Part 3: effects of vibration on structures*. Germany.

Jaksa, M. B., Scott, B. T., Mentha, N. L., Symons, A. T., Pointon, S. M., Wrightson, P. T., et al. (2012). "Quantifying the zone of influence of the impact roller," in International Symposium on Ground Improvement (pp. II-41 to II-52). Brussels: ISSMGE, Brussels, BELGIUM, 31 May – 1 June 2012.

LSTC (2015). *LS-DYNA keyword USER'S manual*. Livermore, California: Livermore Software Technology Corporation.

Scott, B. T., Jaksa, M. B., and Kuo, Y. L. (2012). "Use of proctor compaction testing for deep fill construction using impact rollers," in *Proceedings of international conference on ground improvement & ground control*. Editor C. R. Buddhima Indraratna (Wollongong, Australia: Research Publishing Services), 1107–1112.

Scott, B. T., Jaksa, M. B., and Mitchell, P. (2019a). Ground response to rolling dynamic compaction. *Géotechnique Lett.* 9 (2), 99–105. doi:10.1680/jgele.18.00208

Scott, B. T., Jaksa, M. B., and Mitchell, P. (2019b). "Depth of influence of rolling dynamic compaction," in *Proceedings of the institution of civil engineers - ground improvement*.

Scott, B. T., Jaksa, M. B., and Mitchell, P. (2020). Influence of towing speed on effectiveness of rolling dynamic compaction. *J. Rock Mech. Geotechnical Eng.* 12 (1), 126–134. doi:10.1016/j.jrmge.2019.10.003

Scott, B. T., Jaksa, M. B., and Syamsuddin, E. (2016). "Verification of an impact rolling compaction trial using various *in situ* testing methods," in Proceedings of the 5th International Conference on Geotechnical and Geophysical Site Characterisation, Sydney, Australia, 5-9 September 2016 (Australian Geomechanics Society), 735–740.

Standards Australia (1997). *AS 1289.6.3.2: methods of testing soils for engineering purposes Soil strength and consolidation tests - determination of the penetration resistance of a soil - 9 kg dynamic cone penetrometer test*. Standards Australia.

Standards Australia (1998). *AS 1289.5.5.1: methods of testing soils for engineering purposes Soil compaction and density tests - determination of the minimum and maximum dry density of a cohesionless material - standard method (Reconfirmed 2016)*. Standards Australia.

Standards Australia (2006). *AS 1289.3.5.1: methods of testing soils for engineering purposes Soil classification tests - determination of the soil particle density of a soil - standard method*. Standards Australia.

Standards Australia (2007). *AS 1289.5.8.1: methods of testing soils for engineering purposes Soil compaction and density tests - determination of field density and field moisture content of a soil using a nuclear surface moisture-Density gauge - direct transmission mode*. Standards Australia.

Standards Australia (2009). *AS 1289.3.6.1: methods of testing soils for engineering purposes Soil classification tests - determination of the particle size distribution of a soil - standard method of analysis by sieving*. Standards Australia.

Standards Australia (2016). *AS 1289.6.4.2: methods of testing soils for engineering purposes Soil strength and consolidation tests - determination of compressive strength of a soil - compressive strength of a saturated specimen tested in undrained triaxial compression with measureme*. Standards Australia.

Standards Australia (2017). *AS 1289.5.2.1: methods of testing soils for engineering purposes Soil compaction and density tests - determination of the dry density/moisture content relation of a soil using modified compactive effort*. Standards Australia.

Standards Australia (2020). *AS 1289.6.6.1: methods of testing soils for engineering purposes Soil strength and consolidation tests - Determination of the one-dimensional consolidation properties of a soil - Standard method*. Standards Australia.

10.3389/fbuil.2023.1334090

Nomenclature

c'	effective cohesion
d	depth below ground surface
d'	Drucker-Prager effective cohesion
D	lateral distance to centreline of roller's path
Dr_0	initial relative density
e_0	initial void ratio
e_{max}	maximum void ratio
e_{min}	minimum void ratio
e_L	virgin compression line void ratio intercept
G_s	specific gravity of the solids
L	added vertical loading to each node of the roller
LO	lateral offset
M	Drucker-Prager slope
N	number of passes
p^A	peak applied mean pressure
p_c	apparent preconsolidation pressure
PPA	peak particle acceleration
PPV	peak particle velocity
$\mathbf{PPA}_d$	peak particle acceleration at depth
$\mathbf{PPV}_d$	peak particle velocity at depth
$\mathbf{PPA}_s$	surface peak particle acceleration
$\mathbf{PPV}_s$	surface peak particle velocity
r_i	set of reset offsets
κ	logarithmic slope of unload–reload line
λ	logarithmic slope of virgin compression line
ρ_0	initial bulk density
$\rho_{d\|0}$	initial dry density
σ_h^A	peak applied horizontal stress
σ_L^A	peak applied lateral stress
σ_v^A	peak applied vertical stress
$\varphi_{cv}^{'}$	critical state effective internal angle of friction